Prediction of Progressive Damage and Strength of IM7/977-3 Composites using the Eigendeformation-based homogenization approach: Static Loading.

Michael J. Bogdanor[1] and Caglar Oskay[1]

Abstract

This paper presents the results from the authors' participation in the Air Force Research Laboratory's Damage Tolerance Design Principles Program. The Eigendeformation-based reduced order Homogenization Method (EHM) was employed to predict the mechanical response of a suite of open hole and unnotched IM7/977-3 composite laminates under static tension and compression. Damage accumulation, effective stiffness, and ultimate strength blind predictions are included in addition to the results of the recalibration study. In blind predictions, the proposed multiscale model produced predictions with an average error of 13.1% compared to the experiments for static ultimate strength and 13.6% for stiffness. After recalibration, the average prediction error was improved to 8.7% for static ultimate strength and 4.4% for stiffness. Details of the blind predictions and the recalibration are discussed.

Keywords

Failure prediction, carbon-fiber reinforced composites, multiscale, reduced order, damage modeling

Introduction

The use of composites as structural materials in air vehicles has seen recent and significant growth. This is compounded with rapidly advancing composite materials technology that is allowing the development of new materials at an unprecedented pace. In view of these developments, a rethinking of current aerospace structural design and certification procedures is needed to accelerate time-to-market for composite structural components, while reducing cost. One paradigm shift in this regard is an increased reliance on modeling and simulation in design and certification, with the capability to predict complex damage and failure processes in composite materials and structures. This manuscript reports the capabilities of the *Eigendeformation-based Homogenization Method* (EHM) - a progressive damage analysis approach developed based on multiscale modeling principles. EHM is exercised in predicting the progressive damage accumulation and failure of carbon-fiber reinforced polymer composites subjected to static loading conditions as a part of the Damage Tolerance Design Principles (DTDP) program summarized in this special issue.

Multiscale computational modeling has shown tremendous promise for failure prediction of composite materials and structures. While a number of mathematically robust multiscale computational modeling methodologies have been proposed over the years (e.g., (Hou and Wu 1997; Weinan and Engquist 2003; Ghosh et al. 2001; Oskay 2012, 2013)), computational homogenization-based methods remain among the most popular. Rooted in the mathematical homogenization theory (Babuska 1975; Benssousan et al.

1978; Suquet 1987; Sanchez-Palencia 1980), computational homogenization-based approaches have been employed to study failure in various composite material applications (Terada and Kikuchi 1995; Fish et al. 1997; Miehe et al. 1999; Kouznetsova 2002). In computational homogenization-based approaches, the response at the scale of the composite representative volume element (RVE) or the unit cell is strongly coupled to the macroscopic structure and the two scales are numerically evaluated in a concurrent fashion. Since these approaches rely on explicit resolution of the material microstructure and numerical treatment of the fine scale, composites with arbitrarily complex microstructures (e.g., woven, braided, 3D textile, etc.) can be modeled within the same framework. One important drawback of computational homogenization is that it is computationally very expensive and evaluation of large structural systems using direct computational homogenization is typically not feasible.

EHM (Oskay and Fish 2007; Crouch and Oskay 2010) is a computational homogenization-based modeling approach that has been developed to overcome the issue of high computational cost. EHM is also rooted in the transformation field analysis pioneered by Dvorak and coworkers (Dvorak and Benveniste 1992; Dvorak et al. 1994), and employs the idea of precomputing certain microstructural information

[1]Department of Civil and Environmental Engineering, Vanderbilt University, Nashville, TN 37235, USA

Corresponding author:
Caglar Oskay, Address: VU Station B#351831, 2301 Vanderbilt Place, Nashville, TN 37235, United States
Email: caglar.oskay@vanderbilt.edu

(e.g., localization operators, concentration tensors, influence functions) before the progressive damage and failure analysis at the scale of a structural subelement, element, or component. Nonlinear reduced order microstructural analyses (defined over a unit cell or an RVE), which are coupled to the structural analysis, are then concurrently evaluated for a small subset of unknowns. The precomputed localization operators and concentration tensors, along with the state variables evaluated on-the-fly, are employed to upscale (homogenize) or downscale (localize) the stress and strain fields. EHM can also account for progressive debonding between fiber and matrix at the scale of the microstructure, and is equipped with an adaptive model improvement capability to hierarchically increase model fidelity (Oskay and Fish 2007). EHM has been successfully employed in the prediction of failure under static loading (Crouch and Oskay 2013; Bogdanor and Oskay 2015), blast (Hui and Oskay 2012), compression-after-impact (Yan et al. 2010), and fatigue loading (Crouch and Oskay 2015), as well as failure in thin composite plates (Oskay and Pal 2009; Oskay 2009), in the presence of environmental effects (Krishnan and Oskay 2012), and in the presence of constituent material uncertainty (Bogdanor et al. 2015).

In this manuscript, EHM is employed to predict the failure response of a suite of laminated, unidirectionally reinforced carbon fiber polymer (i.e., IM7/977-3) composite specimens subjected to static loading. The prediction exercise was performed within the timelines of the DTDP program. A detailed description of the DTDP program, including the description of the experiments and composite layups used, is included in a separate publication in this special issue (Clay and Knoth 2016, in review). A particular EHM model was developed for the IM7/977-3 microstructure. The model parameters were calibrated based on experimental results from basic composite laminates provided by the DTDP program for this purpose. The model parameters that describe the elastic behavior and damage evolution of the constituent materials (i.e., fiber and matrix) were identified. The calibrated model was exercised to perform fully blind prediction of the static stiffness, strength, and progressive damage accumulation characteristics of composite laminates with twelve different combinations of layups, geometries, and loading conditons. The specimens were loaded in uniaxial tension and compression and consisted of open hole and unnotched geometries with three separate layups. Upon the completion of the blind prediction phase, the experimental data for the blind prediction cases were received and studied. A recalibration investigation was subsequently performed to improve the capabilities of the EHM model in predicting the failure characteristics of the specimens.

Multiscale Model

The formulation and implementation of the classical homogenization is provided in Reference (Guedes and Kikuchi 1990). The theory, formulation, and computational aspects of EHM are discussed in detail in References (Oskay and Fish 2007) and (Crouch and Oskay 2010). In what follows, a brief description and the governing equations of EHM are provided. In classical computational homogenization, the

effective composite stress-strain behavior at a quadrature point of a nonlinear macroscale analysis is not available in closed form but is computed by numerically solving a boundary value problem defined over the RVE or unit cell of the composite. No explicit failure criteria is defined at the lamina or laminate scale, but rather, macroscale failure is a consequence of the coalescence of damage in the constituent materials within the microstructure. Due to the nonlinearity of the constituents induced by damage accumulation, each quadrature point of the macroscale mesh is associated with a separate RVE, within which, equilibrium and damage evolution must be evaluated, stored, and passed on to the solver of the macroscale problem. EHM introduces a reduced order approximation to the microstructure problem, where a much reduced approximation basis is employed compared to a standard direct numerical (e.g. finite element) solution. This is achieved by first expressing the microscale component of the displacement field in terms of "influence functions," which define its variation over the microstructure. The influence functions are numerical Green's functions computed by solving linear-elastic problems defined over the RVE. The influence functions are computed prior to a progressive damage analysis since they depend only on elastic properties of constituents and microstructure geometry. Next, the inelastic strain field within a microstructure (or eigenstrains in the context of transformation field theory (Dvorak 1992)) are approximated by a coarse discretization. Similar to finite elements, the discretization (i.e., each coefficient) is associated with a subdomain (part) of the microstructure domain. Employing the microscale displacement discretization and the eigenstrain approximation, the microstructure governing equations are converted to an algebraic system, which is solved for the small set of eigenstrain coefficients. The resulting system is computationally much more efficient since the number of unknowns associated with the numerical solution of the microscale RVE problem is much larger than the algebraic system size.

Macroscale problem Let Ω denote the domain of the macrostructure (i.e., specimen domain in this study). The macroscopic equilibrium, kinematic equation, and the boundary conditions are expressed as:

$$\nabla \cdot \bar{\boldsymbol{\sigma}}(\mathbf{x}, t) + \bar{\mathbf{b}}(\mathbf{x}) = 0; \quad \mathbf{x} \in \Omega; \quad t \in [0, t_0] \tag{1}$$

$$\bar{\boldsymbol{\epsilon}}(\mathbf{x}, t) = \nabla^s \bar{\mathbf{u}}(\mathbf{x}, t) \tag{2}$$

$$\bar{\mathbf{u}} = \hat{\mathbf{u}}(\mathbf{x}, t); \quad \mathbf{x} \in \Gamma_u \tag{3}$$

$$\bar{\boldsymbol{\sigma}} \cdot \mathbf{n} = \hat{\mathbf{t}}(\mathbf{x}, t); \quad \mathbf{x} \in \Gamma_t \tag{4}$$

where $\bar{\boldsymbol{\sigma}}$ is the homogenized macroscale stress field, $\bar{\mathbf{b}}$ the body force, $\mathbf{x}$ the spatial coordinate, t the time coordinate, $\bar{\boldsymbol{\epsilon}}$ the homogenized strain, and $\bar{\mathbf{u}}$ the macroscale displacement. $\hat{\mathbf{t}}$ and $\hat{\mathbf{u}}$ denote the boundary tractions and displacements, respectively. $\nabla \cdot ()$ indicates the divergence operator and ∇^s is the symmetric gradient operator.

Microscale problem Let Θ denote the domain of the microstructure (i.e. unit cell RVE in this study). Consider Θ to be comprised of two or more subdomain (or parts), $\boldsymbol{\theta}^{(\gamma)}$, where $\gamma = 1, 2, \ldots, n$ and n is the number of parts. These parts comprise the reduced order model (ROM) of the microstructure. Each part is occupied by a single constituent material and the union of all the parts spans the domain,

$\boldsymbol{\Theta}$. Employing coarse shape functions, the part damage, $\omega^{(\gamma)}$, and part inelastic strain, $\boldsymbol{\mu}^{(\gamma)}$, are taken to be spatially constant over the part (but varying in time). In the EHM analysis, damage evolves separately in each of the parts as a function of the material properties of the constituent material occupying the part, $\boldsymbol{\Psi}^{(\gamma)}$, internal state variables, $\mathbf{s}^{(\gamma)}$, and the localized average strain state in the part, $\boldsymbol{\epsilon}^{(\gamma)}$, (i.e. $\dot{\omega}^{(\gamma)} = f(\boldsymbol{\epsilon}^{(\gamma)}, \mathbf{s}^{(\gamma)}, \boldsymbol{\Psi}^{(\gamma)})$).

The homogenized macroscale stress in Equation 1 over the RVE is computed as:

$$\bar{\boldsymbol{\sigma}} = \sum_{\Delta=1}^{n} \left[1 - \omega^{(\Delta)} \right] \left[\bar{\mathbf{L}}^{(\Delta)} : \bar{\boldsymbol{\epsilon}} + \sum_{\alpha=1}^{n} \bar{\mathbf{P}}^{(\alpha\Delta)} : \boldsymbol{\mu}^{(\alpha)} \right], \quad (5)$$

where ":" denotes the double inner product of two tensors. The unknowns in the microscale boundary value problem are the eigenstrains, $\boldsymbol{\mu}^{(\gamma)}$, which are computed as the solution to the following system of equations:

$$\sum_{\Delta=1}^{n} \left\{ \left[1 - \omega^{(\Delta)} \right] \left[\hat{\mathbf{A}}^{(\alpha\Delta)} : \bar{\boldsymbol{\epsilon}} + \sum_{\gamma=1}^{n} \hat{\mathbf{B}}^{(\alpha\Delta\gamma)} : \boldsymbol{\mu}^{(\gamma)} \right] \right\} = 0$$
$$\forall \alpha = 1, 2, \ldots, n. \quad (6)$$

$\hat{\mathbf{A}}$, $\hat{\mathbf{B}}$, $\bar{\mathbf{L}}$, and $\bar{\mathbf{P}}$ are coefficient tensors computed using the influence functions and elastic constituent properties (Oskay and Fish 2007; Crouch and Oskay 2010).

Damage evolution equations

The evolution of the damage state within part γ of the ROM, $\omega^{(\gamma)}$, is driven by the damage equivalent strain, $\upsilon^{(\gamma)}$, defined as:

$$\upsilon^{(\gamma)} = \sqrt{\frac{1}{2}(\boldsymbol{F}^{(\gamma)}\hat{\boldsymbol{\varepsilon}}^{(\gamma)}) : \hat{\mathbf{L}}^{(\gamma)} : (\boldsymbol{F}^{(\gamma)}\hat{\boldsymbol{\varepsilon}}^{(\gamma)})} \quad (7)$$

in which $\hat{\boldsymbol{\varepsilon}}^{(\gamma)}$ is the vector of principal strains within part γ computed as the eigenvalues of the part strain tensor $\boldsymbol{\epsilon}^{(\gamma)}$, $\hat{\mathbf{L}}^{(\gamma)}$ is the rotated elastic moduli tensor for the constituent material in part γ with respect to the principal strains, and $\boldsymbol{F}^{(\gamma)}$ is the strain weighting matrix that accounts for the tension/compression damage anisotropy. The strain weighting matrix is given as:

$$F^{(\gamma)} = \begin{bmatrix} h_1 & 0 & 0 \\ 0 & h_2 & 0 \\ 0 & 0 & h_3 \end{bmatrix}$$
$$h_\xi = \begin{cases} 1 \text{ if } \hat{\epsilon}_\xi > 0 \\ c^{(\gamma)} \text{ otherwise} \end{cases} \quad \text{for } \xi = 1, 2, 3 \quad (8)$$

where $c^{(\gamma)}$ is the tension/compression anisotropy factor for part γ.

The damage potential, Φ, is computed from the damage equivalent strain following the arctangent evolution function (Oskay and Fish 2004; Fish and Yu 2002):

$$\Phi(\upsilon^{(\gamma)}) = \frac{\arctan(a^{(\gamma)}\langle \upsilon^{(\gamma)} - \upsilon_0^{(\gamma)}\rangle - b^{(\gamma)}) + \arctan(b^{(\gamma)})}{\dfrac{\pi}{2} + \arctan(b^{(\gamma)})}$$
$$(9)$$

where $a^{(\gamma)}$, $b^{(\gamma)}$ and $\upsilon_0^{(\gamma)}$ control the shape of the damage evolution function. To account for the discrepancy in damage evolution between shear-dominated and uniaxial loading,

the parameter controlling the brittleness of failure, $b^{(\gamma)}$, is computed as

$$b^{(\gamma)} = k_b b_s^{(\gamma)} + (1 - k_b)b_n^{(\gamma)} \quad (10)$$

$$k_b = \frac{\gamma_{max}^{(\gamma)}}{\gamma_{max}^{(\gamma)}/2 + \epsilon_{max}^{(\gamma)}}; \quad \in [0, 1] \quad (11)$$

where $b_s^{(\gamma)}$ and $b_n^{(\gamma)}$ are parameters controlling strain to failure in part γ for shear and normal loading, respectively, $\gamma_{\max}$ is the maximum engineering shear strain, and $\epsilon_{\max}$ is the maximum absolute principal strain. For purely shear loading, $k_b = 1$, for purely hydrostatic loading, $k_b = 0$. Damage in the part is then defined as the damage potential of the maximum damage equivalent strain over the loading history:

$$\omega^{(\gamma)} = \Phi(\upsilon_{\max}^{(\gamma)}) \quad (12)$$

where

$$\upsilon_{\max}^{(\gamma)} = \max_{0 \leq \tau \leq t} \{\upsilon^{(\gamma)}(\tau)\}. \quad (13)$$

All parts in the ROM that are comprised of the matrix constituent material take the same set of parameters $\boldsymbol{\Psi}^{(m)} = \{a^{(m)}, b_n^{(m)}, b_s^{(m)}, c^{(m)}, \upsilon_0^{(m)}\}$. The fiber material occupies a single part in the ROM used in this study, which has the set of parameters $\boldsymbol{\Psi}^{(f)} = \{a^{(f)}, b^{(f)}, c^{(f)}, \upsilon_0^{(f)}\}$. The mixed-mode weighting (Equation 10) is not considered for the fiber. Calibration of $\boldsymbol{\Psi}^{(m)}$ and $\boldsymbol{\Psi}^{(f)}$ is described in a later section.

Form of the reduced order model

In this work, the RVE of the microstructure is idealized as a square-packed unit cell with 65% fiber-volume fraction, taken from the experimental average value. The partitioning of the RVE for the EHM model is illustrated in Figure 1. Part 1 is comprised of the entire domain of the fiber and parts 2-4 partition the matrix. Fiber fracture (tensile failure) and crushing (compressive failure) are interpreted from damage accumulation in part 1. Parts 2 and 3, used to describe the matrix material, account for the presence of the disparate failure mechanisms of transverse matrix cracking or crushing and delamination, respectively. Part 4, which also describes the matrix, exhibits damage under both the transverse matrix and delamination failure modes. The coefficient tensors, influence functions, localization operators, and polarization tensors, which define the EHM model, are computed as a preprocessing step before progressive damage analysis. For this microstructure, the use of EHM reduces the model complexity from a finite element model comprised of 416 nodes and 1206 tetrahedral elements to a system with 24 degrees of freedom. The internal state variables required to be stored to represent the damage evolution is also reduced from 1206 in the direct microstructure model to 4 variables in the EHM model.
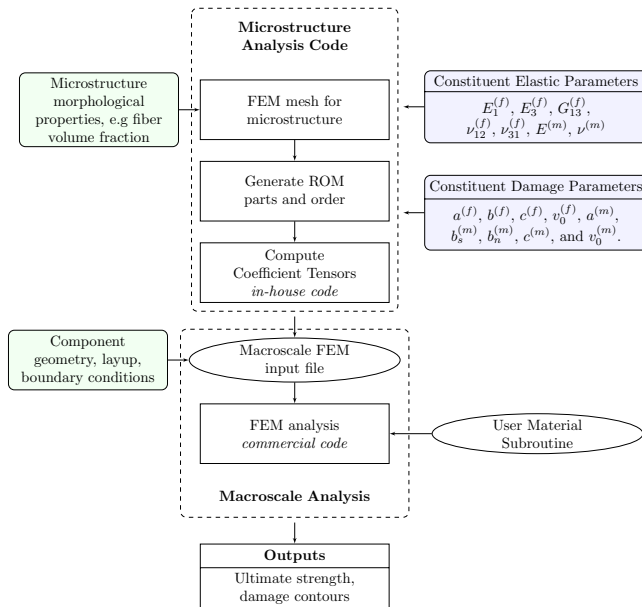
Implementation

Figure 2 outlines the computational implementation strategy and procedure for the evaluation of a composite specimen with EHM. Preprocessing of the composite microstructure is performed using an in house code to generate the parts, construct the EHM model, and compute the associated coefficient tensors. The inputs to the microstructural analysis
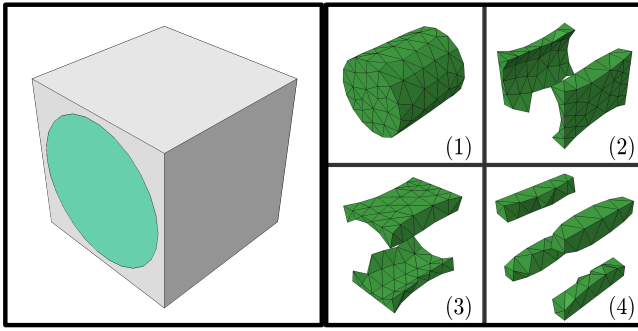
Figure 1. Partitioning of the unidirectionally reinforced composite unit cell.

are the morphology of the unit cell (e.g., fiber volume fraction, cell type) and the constituent material parameters. The coefficient tensor values and the numerical specimen configuration (i.e., layup, orientations, and mesh) are the inputs to the macroscale finite element analysis performed using the commercially available FEM code, Abaqus. The microscale problem is solved at each quadrature point throughout the macroscale analysis using the user material subroutine (UMAT) functionality. The UMAT computes the homogenized secant stiffness tensor and stress at each point. Python scripting is utilized to post-process the information present in the Abaqus output database (i.e., *.odb*) files generated from the numerical simulation. The stress and strain information is extracted from the *.odb* file to produce the stress-strain plots and damage contours are produced through Python scripting and the Abaqus GUI.

Figure 2. Flowchart of the computational implementation of the EHM model in specimen failure prediction.

Calibration, blind prediction and recalibration procedure

In the first phase of this study, a series of blind predictions of laminated composite strength, stiffness, and damage propagation were made using EHM on multiple layups and

loading configurations. A set of composite experiments was provided by the AFRL to calibrate the EHM model for the blind predictions. In the second phase, the experimental results for the blind prediction cases were received and the EHM model was recalibrated. The procedures for the blind prediction and recalibration phases are presented below.

Calibration

Because of the multiscale characteristics of the EHM approach, the associated model parameters are described at the scale of the composite constituents. In contrast, the calibration experiments are provided at the lamina or laminate levels. Calibration of the elastic and damage evolution parameters was therefore performed using a numerical optimization procedure, where the discrete L_2 norm of the differences between the effective composite properties observed in the experiments and those predicted by numerical simulations was minimized. The full suite of calibration experiments conducted at the AFRL are described in full detail elsewhere in this special issue (Clay and Knoth 2016, in review). Among the calibration experiments, six types of experiments were used to calibrate the material parameters: 0° tension, 0° compression, 90° three point bending, 90° compression, ±45° tension, and V-notch shear tests. The effective composite properties defined by these tests are summarized in Table 1.

The EHM model implemented in this work includes seven parameters to fully describe the elastic moduli tensor of the transversely isotropic fiber (i.e., E_1^f, E_3^f, G_{13}^f, ν_{12}^f, and ν_{31}^f) and the isotropic matrix (i.e., E^m and ν^m) where the 3-direction is along the direction of the fiber length, E indicates the Young's modulus, G the shear modulus, and ν the Poisson's ratio. The elastic properties of the fiber and matrix were calibrated to match the mean experimental values reported by the AFRL from the elastic portions of the 0°, ±45°, and 90° three point bend tests. The calibrated constituent parameters are reported in Table 2. The experimental data indicates that the lamina level stiffness of the 0° unidirectionally reinforced specimens was 16.4% lower under compression compared to tension. While the tension-compression anisotropy may be addressed by considering a separate compressive and tensile moduli for the fiber (denoted as E_{3C} and E_{3T}, respectively), all DTDP program participants agreed to proceed without accounting for this anisotropy in the blind prediction phase. In the initial calibration and blind prediction stage, a single longitudinal fiber modulus consistent with the tension tests was chosen. This assumption is revisited in the description of the recalibration of the model.

The accumulation of damage within the fiber is characterized by four model parameters ($a^{(f)}$, $b^{(f)}$, $c^{(f)}$, and $\upsilon_0^{(f)}$), whereas five parameters ($a^{(m)}$, $b_n^{(m)}$, $b_s^{(m)}$, $c^{(m)}$, and $\upsilon_0^{(m)}$) are employed to characterize the matrix damage evolution. Table 2 summarizes the calibrated damage evolution parameters. The experimental data used to calibrate each parameter are also indicated in Table 2. The fiber strength and damage evolution (characterized by $a^{(f)}$, $b^{(f)}$, and $\upsilon_0^{(f)}$) primarily control failure in the 0° tension specimens. The fiber compression anisotropy parameter, $c^{(f)}$, governs failure in the 0° compression specimens. The

Table 1. Comparison of effective composite properties from experiments and blind/recalibrated simulations.

Parameter	Description	Experiment Average	Simulated Value	Calibration Experiment
E_{1t} [GPa]	Long. tension modulus	164.3	163.9	$0°$ tension
E_{1c} [GPa]	*Long. compression modulus*	*137.4*	*137.4*	$0°$ *compression*
E_2 [GPa]	Transverse modulus	8.85	8.85	$90°$ three point bending
G_{13} [GPa]	Shear modulus	4.94	4.94	$\pm45°$ tension
ν_{12}	Long. Poisson's ratio	0.3197	0.321	$0°$ tension
ν_{21}	Transverse Poisson's ratio	0.0175	0.0173	$0°$ tension
X_T [MPa]	Long. tension Strength	2905	2905	$0°$ tension
X_C [MPa]	Long. compression Strength	1274/*1680*	1274/*1680*	$90°$ compression/*Literature*
Y_T [MPa]	Trans. tension Strength	130.0	130.0	$90°$ three point bending
Y_C [MPa]	Trans. compression Strength	247.6	247.7	$90°$ compression

Table 2. Calibrated material properties.

Property	Experiment	Blind Prediction	Recalibration
	Elastic Parameters		
$E_1^{(f)}$ [GPa]	$0°$ Tens.	12.45	12.45
$E_{3T}^{(f)}$ [GPa]	$0°$ Tens.	257.4	257.4
$E_{3C}^{(f)}$ [GPa]	$0°$ Comp.	257.4	215.5
$G_{13}^{(f)}$ [GPa]	$\pm45°$ Tens.	146.0	146.0
$\nu_{12}^{(f)}$	$0°$ Tens.	0.291	0.291
$\nu_{31}^{(f)}$	$0°$ Tens.	0.206	0.206
$E^{(m)}$ [GPa]	$90°$ Tens.	3.70	3.70
$\nu^{(m)}$	$90°$ Tens.	0.37	0.37
	Damage Evolution Parameters		
$a^{(f)}$	$0°$ Tens.	0.04921	0.050562
$b^{(f)}$	$0°$ Tens.	274	274
$c^{(f)}$	$0°$ Comp.	2.3514	1.4481
$v_0^{(f)}$	$0°$ Tens.	1367	1367
$a^{(m)}$	$90°$ 3PB	0.001582	0.001592
$b_n^{(m)}$	$90°$ 3PB	15	15
$b_s^{(m)}$	$\pm45°$ Tens.	-3.2	-3.2
$c^{(m)}$	$90°$ Comp.	0.567	0.535
$v_0^{(m)}$	$90°$ 3PB	636.2	636.2

failure of the $90°$ three point bend tests is predominantly affected by $a^{(m)}$, $b_n^{(m)}$, and $v_0^{(m)}$ and similarly the failure in the $90°$ compression specimens is governed by the matrix compression anisotropy parameter, $c^{(m)}$. The ductility of the $\pm45°$ tension specimens is dictated by the $b_s^{(m)}$ parameter.

Figures 3 and 4 show the comparison of the stress-strain response observed experimentally and computed using the calibrated EHM model. Figure 3 characterizes the unidirectional normal behavior, which is quite brittle. The fiber compression anisotropy parameter, $c^{(f)}$, was calibrated to match the experimental mean of 1274 MPa as reported from the experiments performed at the AFRL (Figure 3(b)). This value was revised in the recalibration phase to reflect higher reported values for this property in literature sources in agreement with all program participants.

Figure 4 shows the $\pm45°$ and V-notch shear behavior which demonstrate significant ductility. For shear cases, the matching was performed up to 10% and 5% strain for the $\pm45°$ tension and V-notch shear cases, respectively, since the experimental data is reliable only up to these strain magnitudes due to strain gage failure (ASTM Standard 3518 2007; ASTM Standard 7078 2005). The agreement between the experiments and simulations is excellent. Table

1 shows the comparison between the specimen level strength and stiffness properties from experiments and numerical simulations, which also demonstrate the accuracy of the calibration.

Blind Prediction

The calibrated EHM model was exercised to predict damage accumulation, stress-strain response, and failure strengths of the $[0,45,90,-45]_{2s}$, $[30,60,90,-60,-30]_{2s}$, and $[60,0,-60]_{2s}$ specimens with open-hole and unnotched configurations under tension and compression. After calibrating the EHM model, the blind prediction phase included constructing the macroscale specimen geometry and discretization for each layup and executing the specimen analysis to obtain the quantities of interest mentioned above.

Details of the Macroscale Model Discretization Twelve macroscale finite element meshes were constructed to model the $[0,45,90,-45]_{2s}$, $[30,60,90,-60,-30]_{2s}$, and $[60,0,-60]_{3s}$ specimens with open-hole and unnotched configurations under tension and compression loading. The numerical specimens were constructed according to the geometry of the gage section in the experiment setups. The finite element meshes of the numerical specimens consisted of elements with a nominal edge length of $h = 1$mm in the in-plane directions and one element per ply in the thickness direction (0.125mm). In order to minimize the effect of mesh density, element size was kept consistent between different numerical specimens. A sensitivity study of mesh density on specimen strength is discussed below.

In order to minimize the effect of mesh bias (i.e., the propensity of damage to propagate along the mesh lines (Song et al. 2011)), the mesh in each ply within a layup was oriented with the fiber direction in the ply. A sample discretization from each of the lamina with an open hole is displayed in Figure 5. This approach to mesh generation and its effect in modeling of composite specimens is discussed in Reference (Song et al. 2011). Since each ply is meshed individually, the nodal positions on the surface of each ply within a stack do not necessarily align. In order to ensure load transfer, the plies were connected using surface tie constraints.
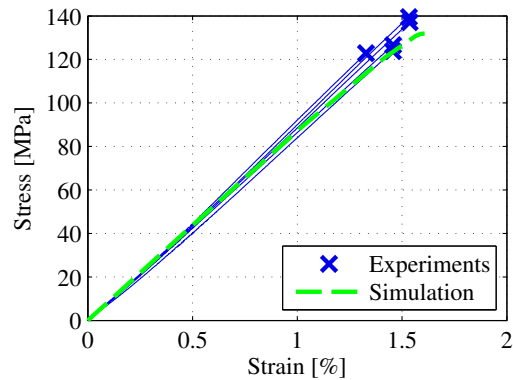
Table 3 displays the mesh characteristics of the numerical specimens. The models used in the blind predictions consisted of 36,000-48,000 trilinear hexahedral elements with full Gauss quadrature (i.e., eight integration points). Only half of the plies in each laminate were modeled, utilizing the symmetry of the layups. In each case,
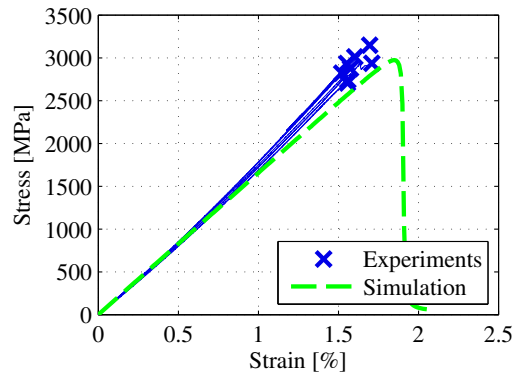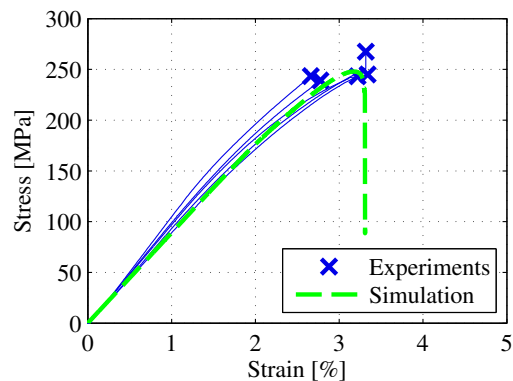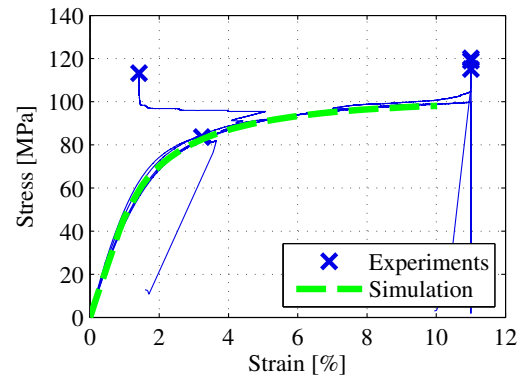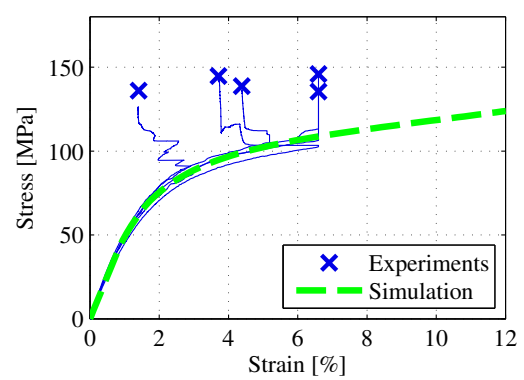
(a)
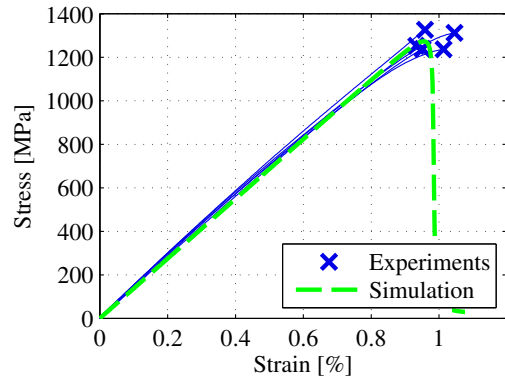
(b)

(c)

(d)

Figure 3. Composite normal stress-strain response from (a) $0°$ tension, (b) $0°$ compression, (c) $90°$ three point bending, and (d) $90°$ compression.


(a)

(b)

Figure 4. Composite shear stress-strain response from (a) $\pm 45°$ tension and (b) V-notch shear.

loading was idealized by applying a pinned boundary condition (i.e. displacement in the specimen longitudinal direction set to zero) at one end of the specimen and applying a monotonically increasing displacement along the longitudinal direction of the opposite end until failure. Strain was computed using a "virtual extensometer" mimicking the extensometer employed in the experiments for the open-hole specimens or the strain gauges in the unnotched specimens. Two nodes in the mesh of the exterior ply in each numerical specimen were identified corresponding to the extensometer ends in the experiments. The simulated strain was reported as the change in the distance between those two nodes divided by the initial separation distance. Stress was computed from the numerical specimens as the sum of the reaction forces at the pinned end of the specimen divided by gross cross-sectional area of the specimen modeled.

The ultimate strength of the simulation is somewhat dependent on the density of the mesh used in the finite element analysis. A mesh sensitivity study was performed in the blind prediction phase to quantify this effect. The effect of mesh density is described below in the context of the $[0, 45, 90, -45]_{2s}$ quasi-isotropic layup with an open-hole configuration subjected to compression loading. The other specimens demonstrated similar trends and are skipped herein for brevity. For comparison with the baseline mesh of $h = 1$mm, a coarser and finer mesh were investigated with edge lengths of 1.5mm and 0.5mm, respectively. A clear trend of a small decrease in the overall strength with decreasing element size was observed in the simulations. The

(a)

(b)

(c)
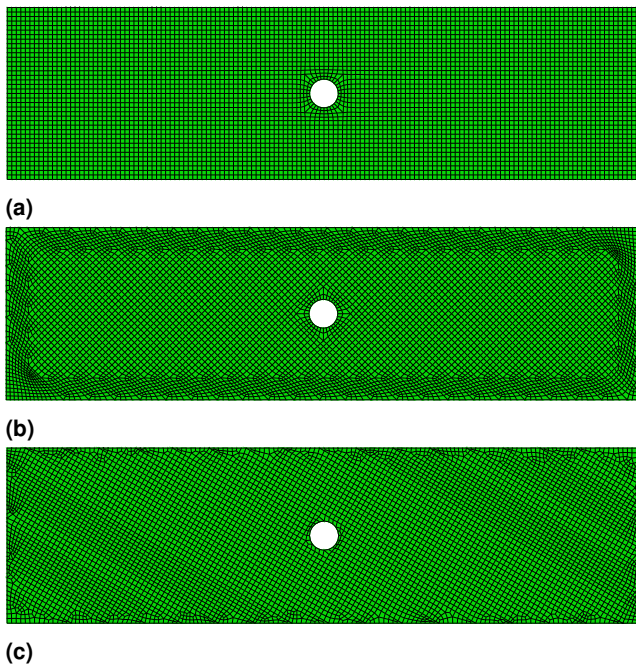
Figure 5. Aligned mesh for (a) $0°/90°$ plies, (b) $\pm45°$ plies, and (c) $\pm30°/60°$ plies used to build the open-hole specimen configurations.

predicted ultimate strength was 344 MPa for the coarse mesh, 335 MPa for the baseline, and 328 MPa for the fine mesh; a difference of 2-3% from the baseline result. This effect is the result of well-known damage localization. Damage contours provided in Figure 6 for 90% of the static ultimate strength demonstrate the damage localization effect where the width of the damage region in the loading direction (vertical on the page) is larger for the coarser mesh and smaller for the fine mesh. In these figures the reduced width of the damage band in the direction of the applied load can be seen, but the overall damage pattern remains similar for all meshes.

Computational Considerations Simulation of the numerical specimens was performed using a parallel computing cluster with 16 2.1GHz AMD Opteron(TM) 6272 Processors and 128 GB shared memory on each compute node. Each of the simulations were performed using 8 cpus on a single compute node in a shared memory parallel configuration. The finite element mesh and wall time for each of the twelve prediction cases is shown in Table 3. In the description of load cases, UNT stands for unnotched tension, OHT for open hole tension, UNC for unnotched compression, and OHC for open hole compression.

Recalibration

Upon submission of the blind prediction results to the AFRL, the experimental data for the twelve experiments were received for recalibration of the EHM model. The purpose of the recalibration was to re-evaluate the assumptions made in the blind prediction phase, make corrections to the model or parameters as necessary, and revise the modeling approach accordingly. The manner in which the initially provided experiments were used to calibrate the multiscale model was assessed and ways in which the model could be improved to better utilize the information from the new experimental

(a) Coarse

(b) Baseline

(c) Fine
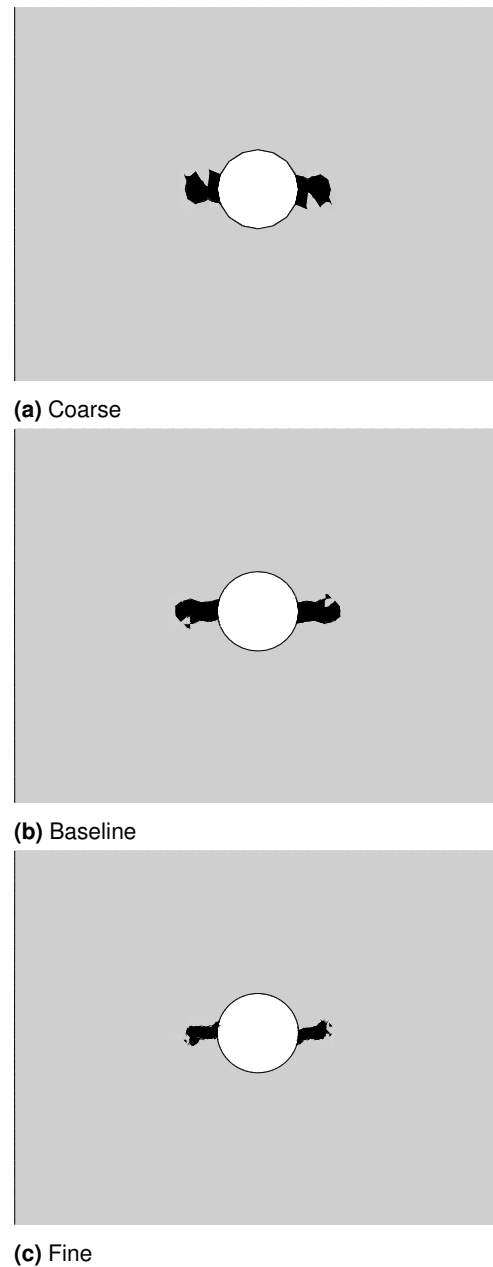
Figure 6. Comparison of transverse matrix damage contours for 90% ultimate stress in $[0, 45, 90, -45]_{2s}$ open-hole compression simulations for the mesh sensitivity study.

Table 3. Numerical specimen mesh sizes and computational wall clock times for failure analysis.

Layup	Case	No. of elements	No. of nodes	Wall time (H:MM)
$[0, 45, 90, -45]_{2s}$	UNT	29264	61216	1:54
$[30, 60, 90, -60, -30]_{2s}$	UNT	40498	84412	2:29
$[60, 0, -60]_{3s}$	UNT	37131	77370	2:15
$[0, 45, 90, -45]_{2s}$	OHT	42652	86896	4:34
$[30, 60, 90, -60, -30]_{2s}$	OHT	53340	108768	4:51
$[60, 0, -60]_{3s}$	OHT	47853	97836	4:09
$[0, 45, 90, -45]_{2s}$	UNC	2744	5876	0:40
$[30, 60, 90, -60, -30]_{2s}$	UNC	3680	7704	0:50
$[60, 0, -60]_{3s}$	UNC	3276	6948	0:47
$[0, 45, 90, -45]_{2s}$	OHC	42652	86896	6:29
$[30, 60, 90, -60, -30]_{2s}$	OHC	53340	108768	7:31
$[60, 0, -60]_{3s}$	OHC	47853	97836	6:17

datasets were identified. Two changes were made to the multiscale model in the recalibration phase in this regard. (1) The tension/compression stiffness anisotropy of the $0°$ composite tape under longitudinal loading was directly accounted for in the EHM model and (2) the effective longitudinal compressive strength of the composite was increased in agreement with all of the program participants. In order to remain consistent across all prediction cases, any change in the model or parameters was applied to the entire suite of blind prediction simulations.

The initial calibration experiments demonstrated a marked discrepancy between the effective longitudinal modulus of the $0°$ unidirectional tape under tension and compression loading. In the recalibration phase, a modeling methodology was developed to directly account for this discrepancy. Since the coefficient tensors associated with the EHM model are functions of the moduli of the fiber and matrix, modeling tension/compression anisotropy requires building a separate model for tensile and compressive cases. The approach is therefore called the dual-ROM approach. The two models vary only in the longitudinal modulus of the transversely isotropic fiber, which is taken to be different for tension and compression, E_{3T}^{f} and E_{3C}^{f}, respectively. The value of E_{3C}^{f} was calibrated based on experimental data from the $0°$ compression tests and the value is included in Table 2. During the analysis of a laminated specimen, some fibers may be subjected to compressive stresses even when the specimen is under overall tensile loading. It is therefore appropriate to consider the compressive ROM in specimen subdomains where the fiber is subjected to compression and the tensile ROM elsewhere. In the current approach, the appropriate model is selected on the fly in the multiscale analysis based on the current state of strain in the fiber direction associated with each quadrature point. Using this approach, a consistent set of parameters was used for each of the twelve specimens. The use of the dual-ROM and directly accounting for the discrepancy between longitudinal tension and compression moduli resulted in a significant improvement in accuracy in the prediction of lamina and laminate level composite stiffnesses across all of the experimental specimens.

An additional recalibration step was implemented to address a perceived experimental issue in the $0°$ compression experiment observed and agreed upon by the team of researchers participating in this study. The $0°$ compression specimens exhibited a significantly lower failure stress compared to data available in the literature for identical or very similar material systems. The team decided to consider the effective longitudinal compression strength to be 1680 MPa compared to the experimentally observed value of 1274 MPa. Challenges in performing the $0°$ compression tests which were used to determine the compression strength value are discussed elsewhere in this special issue (Clay and Knoth 2016, in review). The recalibrated material parameters are shown in Table 2 and the resulting effective composite properties are included in Table 1. The increased longitudinal compression strength improved the overall prediction accuracy, particularly in the compression experiments. A detailed discussion of the results from the blind prediction and recalibration phases is included below.

Results and Discussion

Overall, the EHM model in the blind prediction phase of the program yielded an average error of 13.1% for ultimate strength predictions and 13.6% for predictions of elastic stiffness. The average error was reduced after recalibration to 8.7% for ultimate strength and 4.4% for elastic stiffness predictions. Summaries of the predicted strength and stiffness values from the blind prediction and recalibration phases are provided in Tables 4 and 5. Table 4 includes two sets of results from the recalibration phase. The first column corresponds to the case where only the compression stiffness discrepancy was corrected without a change in the compression strength of the $0°$ undirectional specimens. The second column reflects the effects of both compression stiffness and strength corrections. Accounting for the tension/compression anisotropy in stiffness alone accounted for a 2.7% improvement in the recalibrated prediction of strength and a 9.2% improvement in the prediction of stiffness. The increased compression strength accounted for an additional 1.7% improvement in the prediction of ultimate strength. All improvements reported above are the average of all twelve cases.

$[0,45,90,-45]_{2s}$ Layup

The average prediction error for the quasi-isotropic $[0,45,90,-45]_{2s}$ layup across all configurations was 9.6% and 13.3% for strength and stiffness, respectively, in the blind predictions. This improved to 5.3% and 4.3%, respectively, after recalibration. The stress-strain curves for the $[0,45,90,-45]_{2s}$ open hole and unnotched tension tests are shown in Figure 7. This figure, and the similar subsequent figures for stress and strain, includes the experimental average stress-strain curve to failure, the 90% and 95% confidence bounds on ultimate failure strength as provided by the program coordinators, and the simulated stress-strain curves for the blind prediction, the recalibrated model with $X_c = 1274$ MPa (Recal. A), and the recalibrated model with $X_c = 1680$ MPa (Recal. B). In both blind prediction and recalibration, the EHM model was in very good agreement with the experimentally observed results. In the unnotched tension case (Figure 7a), the blind prediction under-predicted the ultimate strength of the specimen, while the recalibrated model slightly over-predicted the ultimate strength. In both cases, the prediction error was within 7%. For the open-hole specimen (Figure 7b), the blind and recalibrated predictions were within 5% error of the experimental value for ultimate strength. The correction made on the longitudinal compression modulus during the recalibration had a significant impact on the laminate stiffness and strength predictions under tension. This is due to the complex stress states present in the material constituents and points to advantages of using the present multiscale approach where the local stress states are available through localization operations (i.e., $\bar{\sigma} \rightarrow \sigma^{(i)}$). The open-hole simulations demonstrated higher ductility near ultimate strength as compared to the experiments. In continuum damage approaches such as employed herein, damage in a quadrature point represents a loss of stiffness over the entire element. Because this loss of stiffness is not localized to a discrete crack, the width of the region experiencing

Table 4. Summary of predicted ultimate strength for all static simulations.

| | | Ultimate strength over gross cross section [MPa] | | | | | |
| | | | | | Recalibration | | |
Layup	Case	Exp.	Blind Prediction		$X_c = 1274$MPa		$X_c = 1680$MPa	
$[0, 45, 90, -45]_{2s}$	UNT	866	807	-6.9%	896	+3.5%	911	+5.2%
$[30, 60, 90, -60, -30]_{2s}$	UNT	473	582	+23.0%	492	+4.0%	522	+10.3%
$[60, 0, -60]_{3s}$	UNT	1005	802	-20.2%	1012	+0.7%	1014	+0.9%
$[0, 45, 90, -45]_{2s}$	OHT	554	529	-4.5%	542	-2.2%	558	+0.7%
$[30, 60, 90, -60, -30]_{2s}$	OHT	409	423	+3.5%	453	+10.8%	449	+9.8%
$[60, 0, -60]_{3s}$	OHT	543	498	-8.2%	487	-10.3%	502	-7.6%
$[0, 45, 90, -45]_{2s}$	UNC	605	451	-25.5%	474	-21.7%	605	0.0%
$[30, 60, 90, -60, -30]_{2s}$	UNC	392	368	-6.1%	349	-11.0%	425	+8.4%
$[60, 0, -60]_{3s}$	UNC	765	437	-42.9%	469	-38.7%	602	-21.4%
$[0, 45, 90, -45]_{2s}$	OHC	341	335	-1.8%	326	-4.4%	393	+15.2%
$[30, 60, 90, -60, -30]_{2s}$	OHC	295	299	+1.4%	296	+0.3%	360	+22.0%
$[60, 0, -60]_{3s}$	OHC	358	311	-13.1%	297	-17.2%	368	+2.8%
		Avg. abs. error	13.1%		10.4%		8.7%	

Table 5. Summary of predicted stiffness for all static simulations.

| | | Stiffness [GPa] | | | | |
Layup	Case	Experiment	Blind Prediction		Recalibration	
$[0, 45, 90, -45]_{2s}$	UNT	60.5	61.52	+1.7%	60.41	-0.1%
$[30, 60, 90, -60, -30]_{2s}$	UNT	38.0	40.59	+6.8%	39.84	+4.8%
$[60, 0, -60]_{3s}$	UNT	59.5	62.13	+4.4%	61.68	+3.7%
$[0, 45, 90, -45]_{2s}$	OHT	48.3	51.72	+7.1%	50.84	+5.3%
$[30, 60, 90, -60, -30]_{2s}$	OHT	32.4	35.40	+9.3%	34.57	+6.7%
$[60, 0, -60]_{3s}$	OHT	48.8	51.88	+6.3%	50.84	+4.2%
$[0, 45, 90, -45]_{2s}$	UNC	48.0	61.52	+28.2%	52.80	+10.0%
$[30, 60, 90, -60, -30]_{2s}$	UNC	33.5	40.59	+21.2%	34.41	+2.7%
$[60, 0, -60]_{3s}$	UNC	48.9	62.13	+27.0%	52.36	+7.1%
$[0, 45, 90, -45]_{2s}$	OHC	44.5	51.72	+16.2%	45.22	+1.6%
$[30, 60, 90, -60, -30]_{2s}$	OHC	30.1	35.40	+17.6%	31.76	+5.5%
$[60, 0, -60]_{3s}$	OHC	44.4	51.88	+16.8%	44.77	+0.8%
	Avg. abs. error		13.6%		4.4%	

the stiffness loss is larger than in the physical specimen, which accounts for the artificially higher degree of ductility witnessed in the simulations as compared to the experiments.

In the compression cases for the [0,45,90,-45]$_{2s}$ layup, the effect of the recalibration is pronounced. In Figure 8a, the prediction of stiffness is significantly improved through the use of the dual-ROM and directly accounting for the disparity between the longitudinal compression and tension moduli. In the blind predictions, the stiffness of the unnotched compression test had 28.2% error. After recalibration, this error in the stiffness was reduced to 10.0%. In the open hole specimens (Figure 8b), the error in the stiffness was reduced from 16.2% to 1.6%. The effect of using the higher value for longitudinal compression strength (Recal. B) is observed in both the unnotched and open hole compression cases. In the unnotched compression case, using $X_c = 1680$MPa reduced the error in the prediction from over 20% to an error of less than 1% compared to the experiments. In the open hole compression case however, the strength prediction error increased from 1.8% to 15.1%. In both compression cases, using the higher value of lamina compression strength increased the ultimate strength of the laminate, as expected. The increased error in the open hole compression case is a result of using the consistent model

through all twelve prediction cases, which in this case did not improve the prediction result. The additional nonlinearity near ultimate failure is also observed in the open hole compression tests.

Damage contour plots from the recalibrated multiscale analysis (Recal. B) are compared to the experimental X-ray computed tomography (CT) images at 90% of the static ultimate strength of the [0,45,90,-45]$_{2s}$ open hole tension experiment in Figure 9 (The predicted damage patterns did not change significantly from the blind predictions to the recalibrated simulations, thus for brevity only the recalibrated results are shown). Due to the partitioning of the ROM, it is possible to directly interpret separate failure modes in the composite from the presence of damage in the different ROM parts as shown in Figure 1. Fiber failure at a quadrature point corresponds to damage in part 1 of the ROM reaching unity. Matrix cracking and delamination are similarly interpreted from damage values in parts 2 and 3, respectively. When the corresponding damage values reach unity in an element, the entire element is highlighted as shown in Figure 9. Damage in the [0,45,90,-45]$_{2s}$ open hole layup under tension is dominated by transverse matrix cracking around the hole, primarily in the 90° and ±45° plies. The damage initiates near the hole and extends outward

(a)

(b)
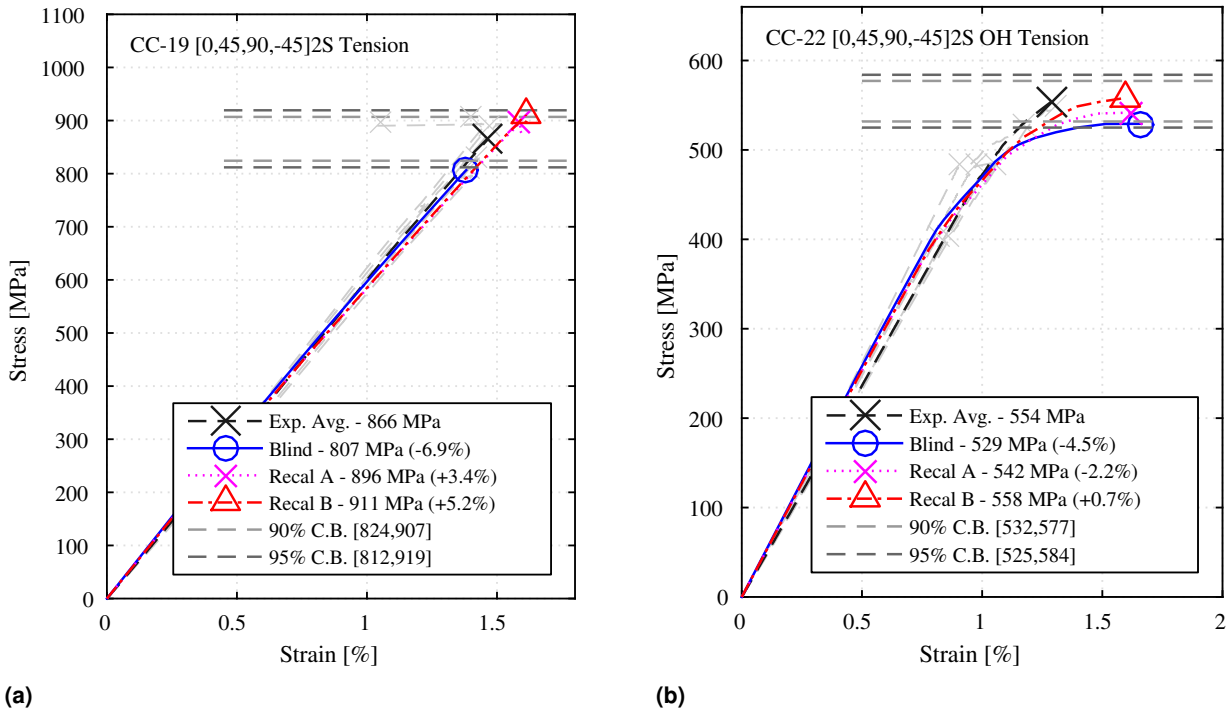
Figure 7. [0,45,90,-45]$_{2s}$ (a) unnotched and (b) open-hole tension experiments and blind and recalibrated simulations.


(a)

(b)
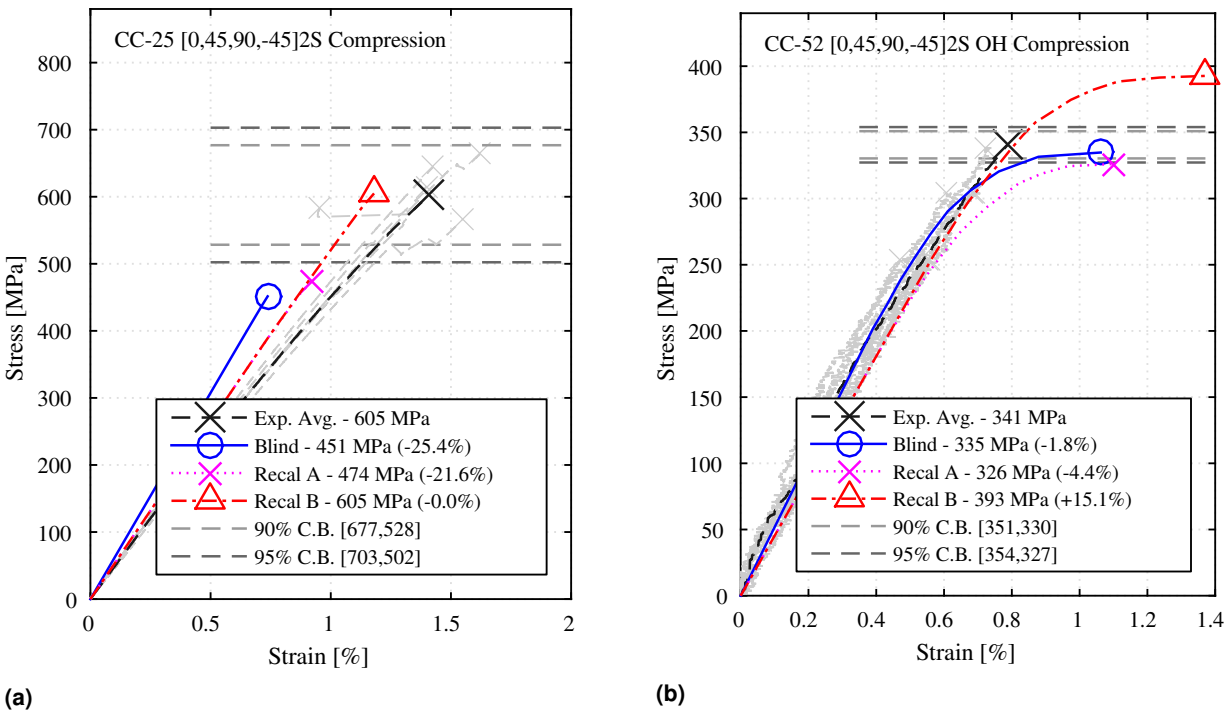
Figure 8. [0,45,90,-45]$_{2s}$ (a) unnotched and (b) open-hole compression experiments and blind and recalibrated simulations. The x and y-axes in the figures indicate compressive strains and stresses, respectively.

in the direction of fibers in each of the 90° and ±45° plies. In the ±45° plies, some additional damage accumulation propagating transverse to the fiber direction was predicted. A small amount of matrix damage around the hole in the 0° plies is also observed, indicating the presence of fiber splitting. This matrix damage behavior is consistent between the simulated damage contours and the CT images. The small amount of fiber failure at the hole in the 0° plies predicted in the simulations does not appear in the CT

images. The simulation also predicts a small amount of delamination around the hole, predominantly near the 0° plies. The presence of such delaminations can be seen in the CT images as well.

[30,60,90,-60,-30]$_{2s}$ Layup

The [30,60,90,-60,-30]$_{2s}$ layup is a "soft" layup that contains no 0° plies. The strength of this layup is therefore markedly lower than the other two layups. The average error in
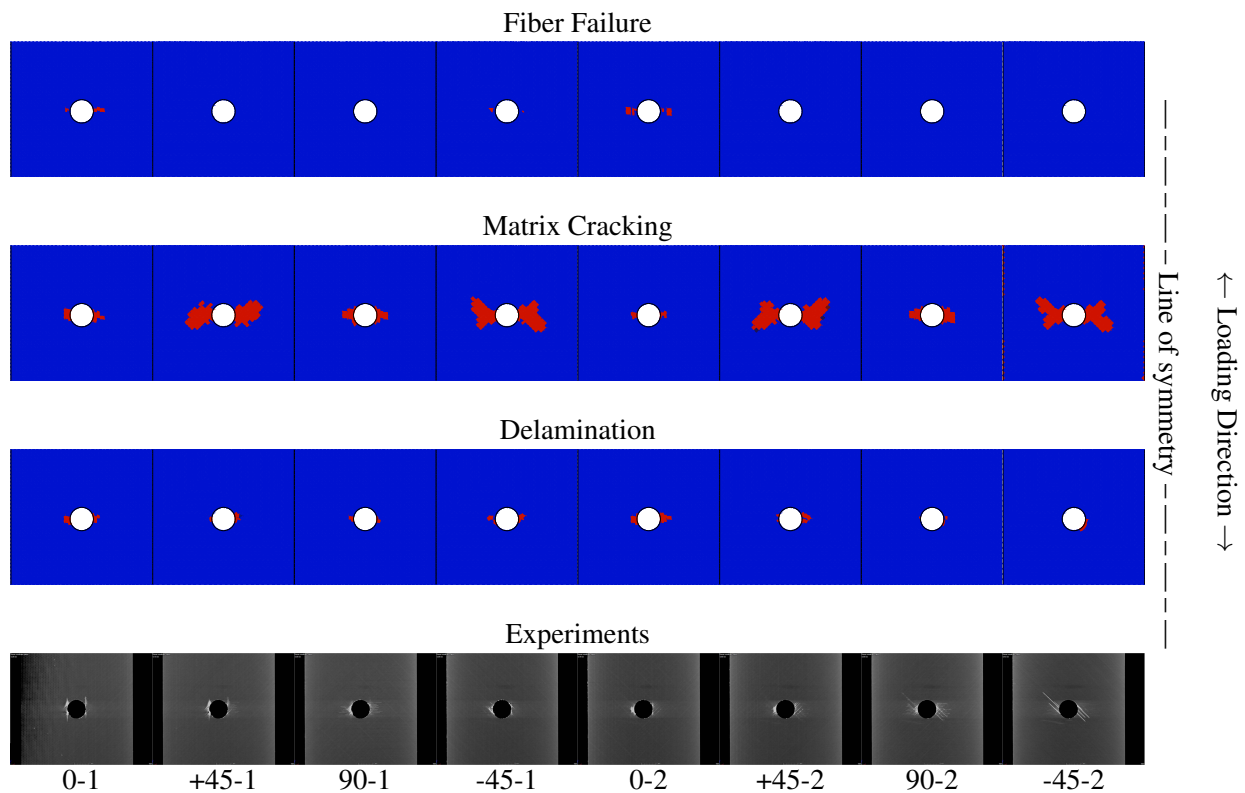
Figure 9. Static damage contours for [0,45,90,-45]$_{2s}$ layup at 90% ultimate strength.

this layup increased from 8.5% to 12.7% in terms of ultimate strength predictions after full recalibration using the increased longitudinal compression strength (Recal. B). Using the original longitudinal compression strength value of 1274 MPa and only accounting for the tension/compression anisotropy of the effective longitudinal elastic stiffness (i.e., Recal. A), the average error in laminated strength was reduced to 6.5%. The recalibration improved the average error in the prediction of the laminate stiffness for the [30,60,90,-60,-30]$_{2s}$ layups from 13.7% in the blind predictions to 4.9%. The impact of the longitudinal compression strength and elastic modulus on this soft layup is significant, given that the layup contains no 0° plies. The ultimate strength was over-predicted in blind prediction and after recalibration in both the open hole and unnotched tension tests of the [30,60,90,-60,-30]$_{2s}$ layup, as shown in Figure 10. The reduced effective longitudinal compression modulus value in recalibration reduced the ultimate strength prediction for the unnotched specimen (Figure 10a) and increased the ultimate strength prediction in the open hole specimen (Figure 10b). In both cases, the prediction error after recalibration was approximately 10%.

In the [30,60,90,-60,-30]$_{2s}$ compression tests shown in Figure 11, the accuracy of the predicted stiffness was significantly improved after recalibration from errors of 21.2% and 17.6% for the unnotched and open hole compression tests, respectively, to 2.7% and 5.5%, respectively, after recalibration (Recal. B). The increased longitudinal compression strength after recalibration resulted in a slightly larger prediction error in the [30,60,90,-60,-30]$_{2s}$ layups under compression loading.

Figure 12 displays the damage contour comparison between the recalibrated simulation and the experiments at 90% of the ultimate static strength of the specimen. Similar to the [0,45,90,-45]$_{2s}$ layup, the dominant failure mode is transverse matrix cracking. In the ±60° plies, the matrix is completely failed in the load ligament regions. There is also significant matrix damage in the ±30° and 90° plies both originating at the open hole and at the edges of the specimen. Minor delamination regions are predicted around the hole in each ply as well.

[60,0,-60]$_{3s}$ Layup

Figure 13 shows the tensile loading results for the [60,0,-60]$_{3s}$ specimen with the unnotched and open-hole configurations. The initially reported blind prediction for the strength of the unnotched tension case was 802 MPa, with 20.2% error compared to the experiments. The strength predictions of the recalibrated model were 1012 and 1014 MPa for Recal. A and Recal. B, respectively, with less than 1% error. It was determined that the primary discrepancy between the blind prediction and the recalibrated model is due to an error made during the reporting of the blind prediction cases to the DTDP program. The correct predicted strength in the blind prediction (with parameters reported in this manuscript for the blind prediction case) is 1050 MPa, with 4.5% error. In the interest of the program objectives, the present article only reports the blind predictions and recalibrations reported to the program. In the [60,0,-60]$_{3s}$ open hole tension specimen, recalibration of the model did not significantly alter the prediction result. In all cases for the open hole tension specimen, the prediction error was between 7.6% and 10.3% (see Figure 13b).
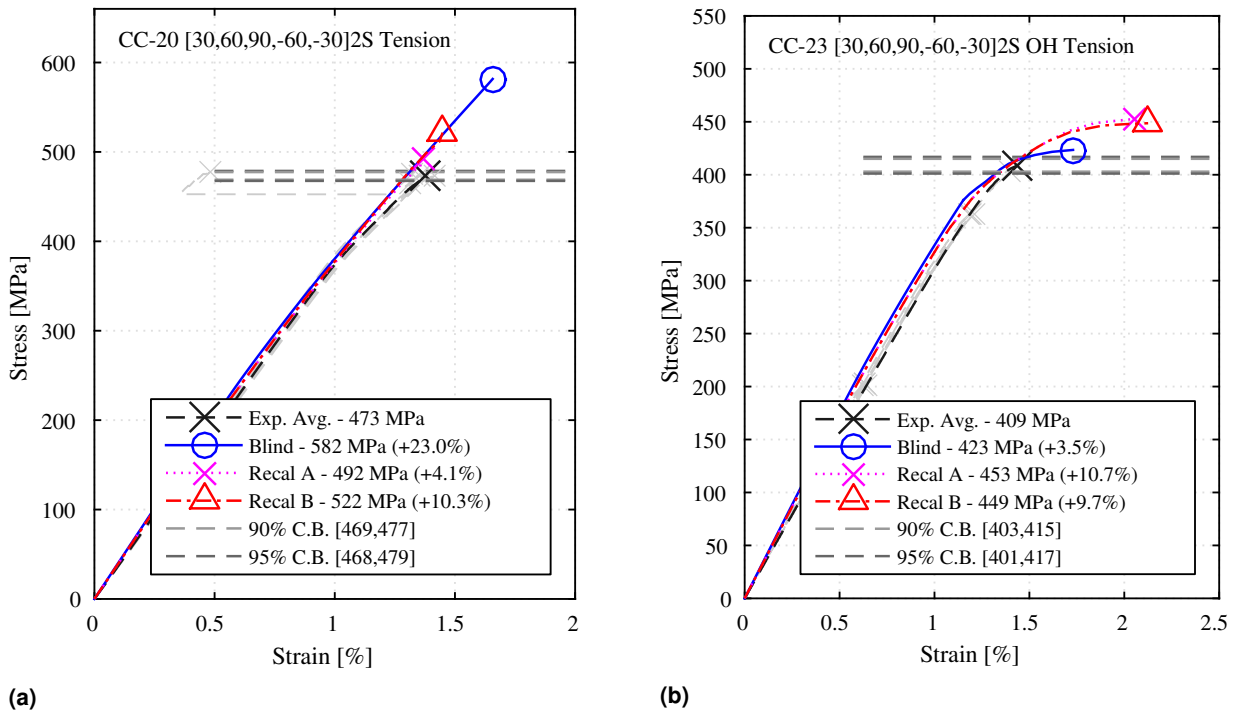
Figure 10. $[30,60,90,-60,-30]_{2s}$ (a) unnotched and (b) open-hole tension experiments and blind and recalibrated simulations.
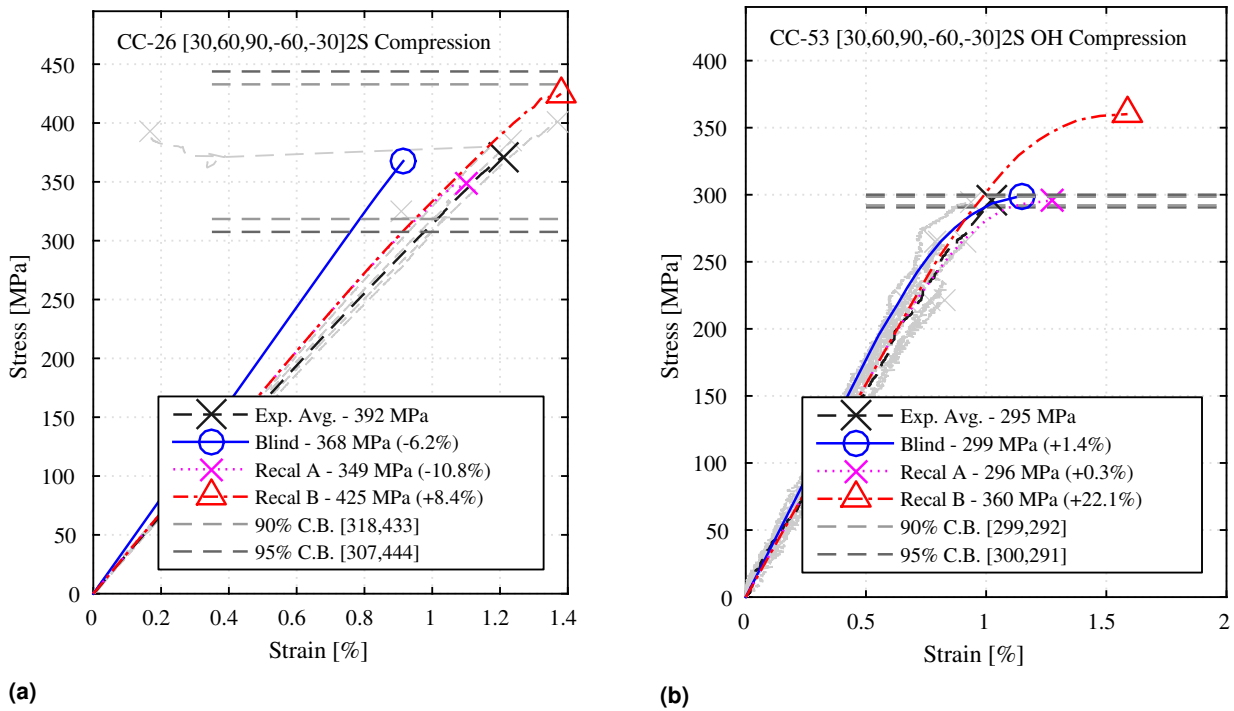
Figure 11. $[30,60,90,-60,-30]_{2s}$ (a) unnotched and (b) open-hole compression experiments and blind and recalibrated simulations. The x and y-axes in the figures indicate compressive strains and stresses, respectively.

The ultimate strength of the $[60,0,-60]_{3s}$ unnotched compression test was under-predicted by a large margin in both blind prediction and recalibration, as displayed in Figure 14a. The blind prediction had 42.9% error and after recalibration the error improved to 21.3%. This case represented the largest prediction error for all twelve specimens. The prediction of the $[60,0,-60]_{3s}$ open hole compression strength in Figure 14b was significantly

improved in recalibration from 13.1% in blind prediction to 2.8% after recalibration.

The damage contour plots for the $[60,0,-60]_{3s}$ specimen with the open hole in tension at 90% of the ultimate static strength are displayed in Figure 15 for both the recalibrated prediction and the experiments. In the simulation of damage evolution, the accumulation of transverse matrix damage is significantly over-predicted in the $\pm 60°$ plies as compared with the experiments. The higher degree of
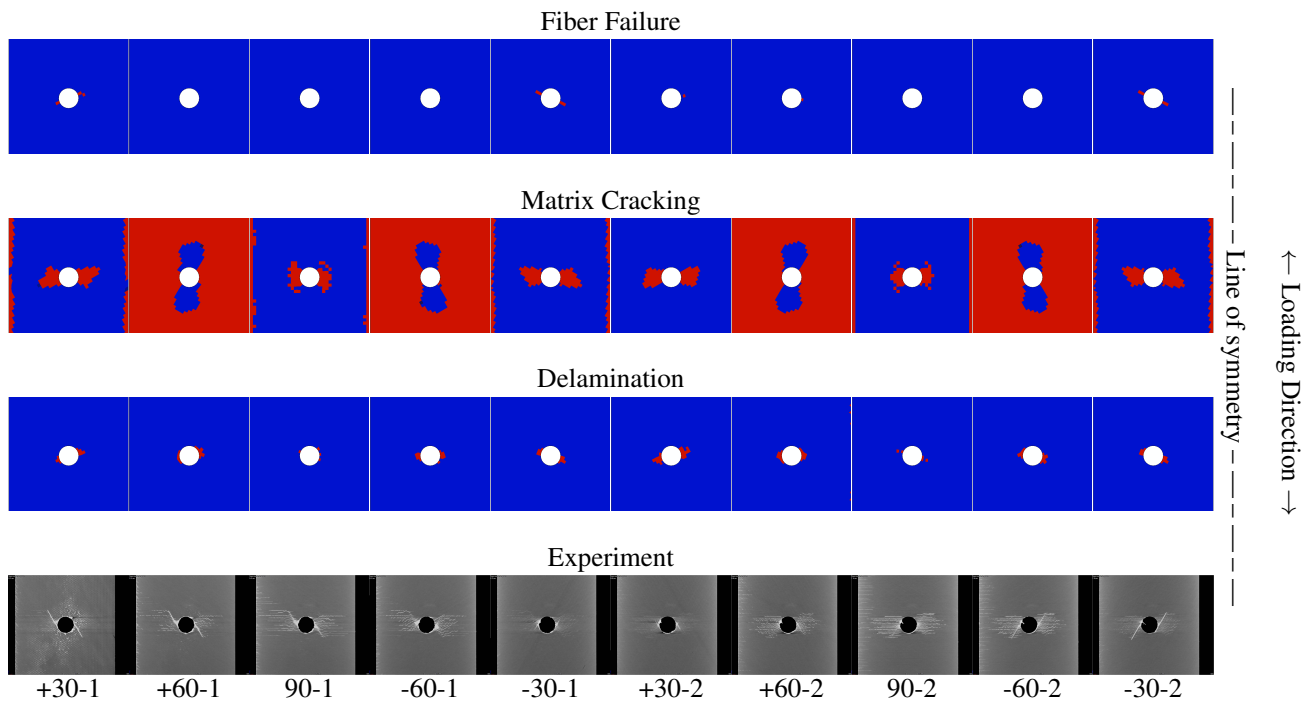
Figure 12. Static damage contours for $[30,60,90,-60,-30]_{2s}$ layup at 90% ultimate strength.

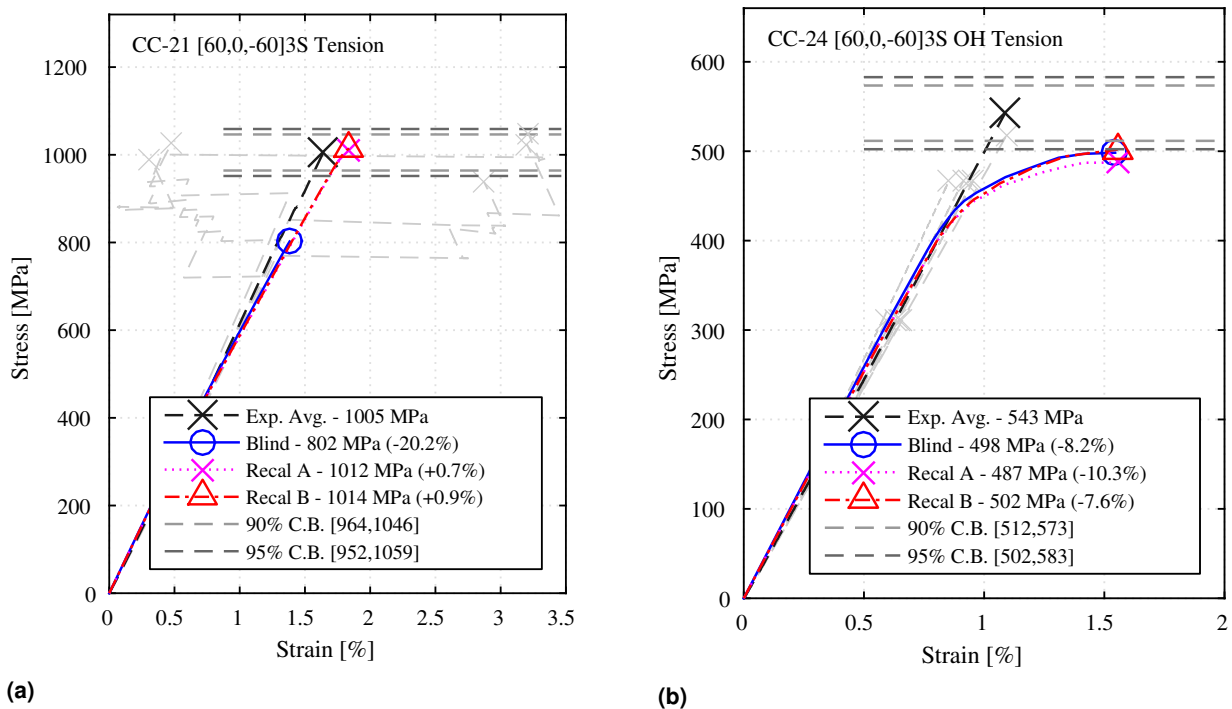**(a)**   **(b)**
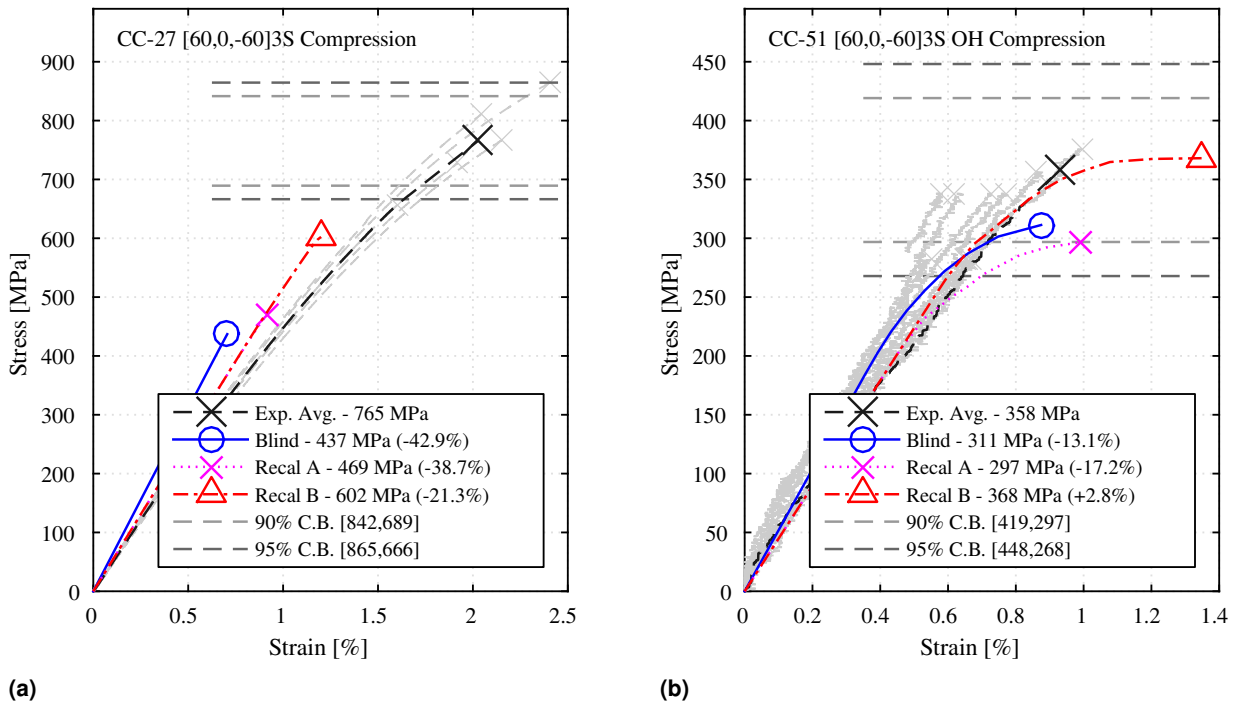
Figure 13. $[60,0,-60]_{3s}$ (a) unnotched and (b) open-hole tension experiments and blind and recalibrated simulations.

ductility observed in the prediction of stress-strain curves are consistent and caused by this over-predicted damage extent in the simulations. Matrix cracks are observed in the CT images, but at a lesser degree than in the prediction. The simulation does predict the accumulation of transverse matrix cracks in the 0° plies adjacent to the hole, accompanied by small regions of delamination. This is consistent with the vertical fiber splitting cracks observed in the CT images adjacent to the open hole in the 0° plies. The simulation also predicts the initiation of fiber failure in the

0° plies near the open hole at the 90% ultimate strength load.

Conclusion

The EHM model predictions of damage accumulation, stiffness, and ultimate strength of a range of laminated composite layups under tension and compression in this program have been satisfactory. The EHM model was able to accurately and efficiently upscale damage laws for the constituents at the microscale to the macroscale

(a)   **(b)**

Figure 14. [60,0,-60]$_{3s}$ (a) unnotched and (b) open-hole compression experiments and blind and recalibrated simulations. The x and y-axes in the figures indicate compressive strains and stresses, respectively.
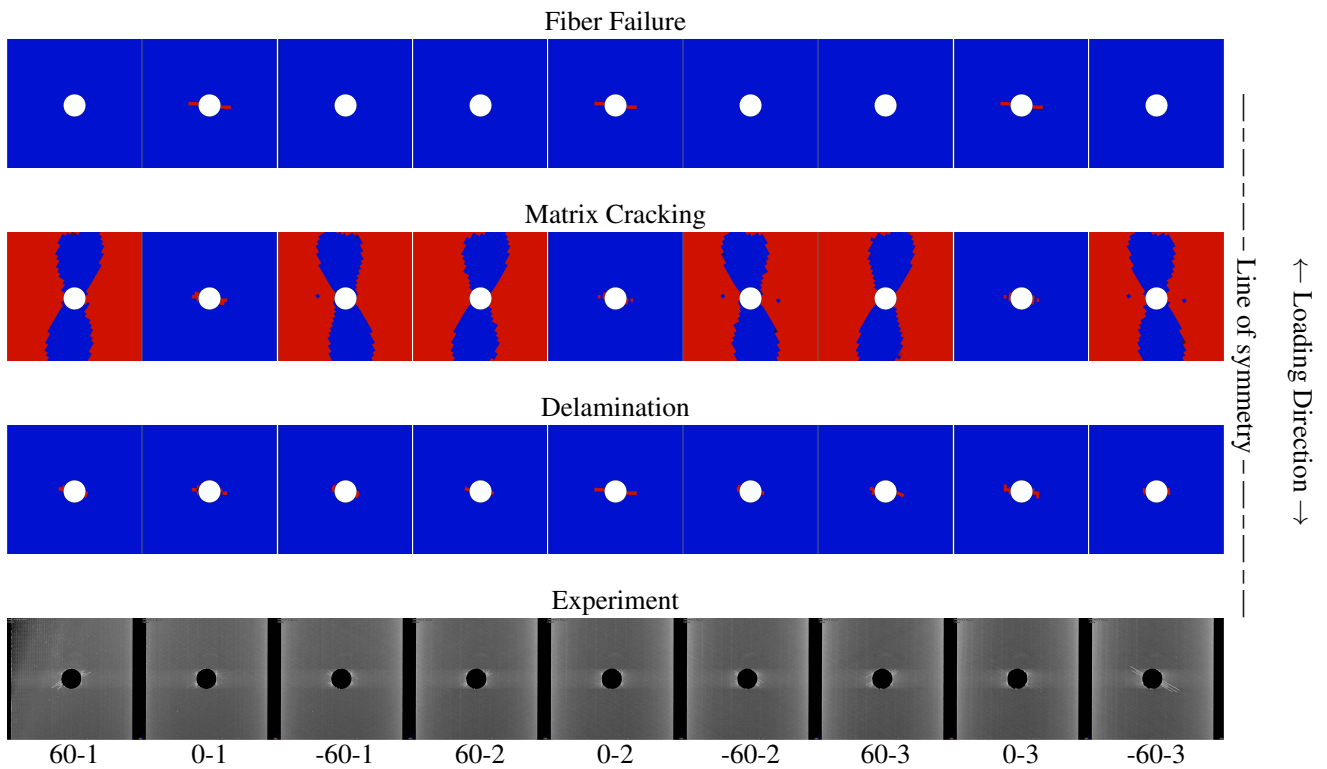
Figure 15. Static damage contours for [60,0,-60]$_{3s}$ layup at 90% ultimate strength.

analysis of the laminated composite test specimens. Elastic and damage evolution parameters for the fiber and matrix constituents were calibrated using the experimental data provided by the AFRL. In static blind predictions, ultimate strength predictions with an average error of 13.1% from the experiments and an average stiffness error of 13.6% were produced. In recalibration, the effective composite longitudinal modulus tension/compression anisotropy was

taken into account in the microscale model and the longitudinal compression strength of the 0° unidirectional tape was increased to a value in better agreement with other literature sources. The resulting recalibrated predictions demonstrated an average ultimate strength error of 8.7% and an average stiffness error of 4.4%. Damage contour plots displaying fiber failure, transverse matrix cracking, and delamination failure were also compared with

the experimental CT images for the open hole tension specimens.

The future efforts in advancing the EHM methodology will focus on eliminating the mesh sensitivity and mesh bias issues in a computationally efficient manner. While a number of approaches exist to alleviate these issues, they often rely on very fine discretization of the specimen domains. This often leads to unacceptable computational costs for large structural analyses. An efficient, mesh insensitive modeling framework will make a dramatic impact on fidelity of EHM (and many other progressive damage analysis) simulations.

Acknowledgements

References

ASTM Standard 3518. Standard test method for in-plane shear response of polymer matrix composite materials by tensile test of a +/-45° laminate. ASTM International, West Conshohocken, PA, 2007.

ASTM Standard 7078. Standard test method for shear properties of composite materials by v-notched rail shear method. ASTM International, West Conshohocken, PA, 2005.

I. Babuska. Homogenization and application. mathematical and computational problems. In B. Hubbard, editor, *Numerical Solution of Partial Differential Equations - III, SYNSPADE.* Academic Press, 1975.

A. Benssousan, J. L. Lions, and G. Papanicolaou. *Asymptotic Analysis for Periodic Structures.* North-Holland, Amsterdam, 1978.

M.J. Bogdanor and C. Oskay. Application of reduced order multiscale homogenization to assess and quantify the benefits of applying damage tolerant design principles to advanced composite aircraft structures. *Proceedings of the 56th AIAA Structures, Structural Dynamics, and Materials*, 2015.

M.J. Bogdanor, C. Oskay, and S.B. Clay. Multiscale modeling of failure in composites under model parameter uncertainty. *Comput. Mech.*, 56:389–404, 2015.

S.B. Clay and P.M. Knoth. Experimental results of static testing for calibration and validation of composite progressive damage analysis methods. *J. Compos. Mater.*, 2016, in review.

R. Crouch and C. Oskay. Symmetric mesomechanical model for failure analysis of heterogeneous materials. *Int. J. Multiscale Comp. Eng.*, 8:447–461, 2010.

R. Crouch and C. Oskay. Experimental and computational investigation of progressive damage accumulation in CFRP composites. *Compos. Part B-Eng.*, 48:59–67, 2013.

R. Crouch and C. Oskay. Accelerated time integrator for multiple time scale homogenization. *Int. J. Numer. Meth. Eng.*, 101: 1019–1042, 2015.

G. J. Dvorak. Transformation field analysis of inelastic composite materials. *Proc. Roy. Soc. London Ser. A*, 437:311–327, 1992.

G. J. Dvorak and Y. Benveniste. On transformation strains and uniform fields in multiphase elastic media. *Proc. Roy. Soc. London Ser. A*, 437:291–310, 1992.

G.J. Dvorak, A.M. Wafa, and Y.A. Bahei-El-Din. Implementation of the transformation field analysis for inelastic composite materials. *Comput. Mech.*, 14:201–228, 1994.

J. Fish and Q. Yu. Computational mechanics of fatigue and life predictions for composite materials and structures. *Comput. Meth. Appl. Mech. Eng.*, 191:4827–4849, 2002.

J. Fish, K. Shek, M. Pandheeradi, and M. S. Shephard. Computational plasticity for composite structures based on mathematical homogenization: Theory and practice. *Comput. Meth. Appl. Mech. Eng.*, 148:53–73, 1997.

S. Ghosh, K. Lee, and P. Raghavan. A multi-level computational model for multi-scale damage analysis in composite and porous materials. *Int. J. Solids Struct.*, 38:2335–2385, 2001.

J. M. Guedes and N. Kikuchi. Preprocessing and postprocessing for materials based on the homogenization method with adaptive finite element methods. *Comput. Meth. Appl. Mech. Eng.*, 83: 143–198, 1990.

T. Y. Hou and X.-H. Wu. A multiscale finite element method for elliptic problems in composite materials and porous media. *J. Comput. Phys.*, 134:169–189, 1997.

T. Hui and C. Oskay. Computational modeling of polyurea-coated composites subjected to blast loads. *J. Compos. Mater.*, 46: 2167–2178, 2012.

V. G. Kouznetsova. *Computational Homogenization for the multi-scale Analysis of multi-phase materials.* 2002.

A. Krishnan and C. Oskay. Modeling compression-after-impact response of polymer matrix composites subjected to seawater aging. *J. Compos. Mater.*, 46:2851–2861, 2012.

C. Miehe, J. Schröder, and J. Schotte. Computational homogenization analysis in finite plasticity simulation of texture development in polycrystalline materials. *Comput. Meth. Appl. Mech. Eng.*, 171:387–418, 1999.

C. Oskay. Two-level multiscale enrichment methodology for modeling of heterogeneous plates. *Int. J. Numer. Meth. Eng.*, 80:1143–1170, 2009.

C. Oskay. Variational multiscale enrichment for modeling coupled mechano-diffusion problems. *Int. J. Numer. Meth. Eng.*, 89: 686–705, 2012.

C. Oskay. Variational multiscale enrichment method with mixed boundary conditions for modeling diffusion and deformation problems. *Comp. Meth. Appl. Mech. Eng.*, 264:178–190, 2013.

C. Oskay and J. Fish. Fatigue life prediction using 2-scale temporal asymptotic homogenization. *Int. J. Numer. Meth. Eng.*, 61:329–359, 2004.

C. Oskay and J. Fish. Eigendeformation-based reduced order homogenization for failure analysis of heterogeneous materials. *Comput. Meth. Appl. Mech. Eng.*, 196:1216–1243, 2007.

C. Oskay and G. Pal. A multiscale failure model for analysis of thin heterogeneous plates. *Int. J. Damage Mech.*, 19:575–610, 2009.

E. Sanchez-Palencia. *Non-homogeneous media and vibration theory*, volume 127 of *Lecture notes in physics*. Springer-Verlag, Berlin, 1980.

K. Song, Y. Li, and C. A. Rose. Continuum damage mechanics models for the analysis of progressive failure in open-hole

tension laminates. *52nd AIAA Structures Structural Dynamics and Materials Conference*, 1861:1–18, 2011.

P. M. Suquet. Elements of homogenization for inelastic solid mechanics. In E. Sanchez-Palencia and A. Zaoui, editors, *Homogenization Techniques for Composite Media*. Springer-Verlag, 1987.

K. Terada and N. Kikuchi. Nonlinear homogenization method for practical applications. In S. Ghosh and M. Ostoja-Starzewski, editors, *Computational Methods in Micromechanics*, volume AMD-212/MD-62, pages 1–16. ASME, 1995.

E. Weinan and B. Engquist. The heterogenous multiscale methods. *Commun. Math. Sci.*, 1:87–132, 2003.

H. Yan, C. Oskay, A. Krishnan, and L.R. Xu. Compression after impact response of woven fiber-reinforced composites. *Compos. Sci. Technol.*, 70:2128–2136, 2010.